



A Survey of Nanoflare Properties in Active Regions Observed with the *Solar Dynamics Observatory*

Nicholeen M. Viall and James A. Klimchuk

NASA Goddard Space Flight Center, Solar Physics Laboratory, Greenbelt, MD 20771, USA

Received 2017 March 21; revised 2017 May 2; accepted 2017 May 2; published 2017 June 20

Abstract

In this paper, we examine 15 different active regions (ARs) observed with the *Solar Dynamics Observatory* and analyze their nanoflare properties. We have recently developed a technique that systematically identifies and measures plasma temperature dynamics by computing time lags between light curves. The time lag method tests whether the plasma is maintained at a steady temperature, or if it is dynamic, undergoing heating and cooling cycles. An important aspect of our technique is that it analyzes both observationally distinct coronal loops as well as the much more prevalent diffuse emission between them. We find that the widespread cooling reported previously for NOAA AR 11082 is a generic property of all ARs. The results are consistent with impulsive nanoflare heating followed by slower cooling. Only occasionally, however, is there full cooling from above 7 MK to well below 1 MK. More often, the plasma cools to approximately 1–2 MK before being reheated by another nanoflare. These same 15 ARs were first studied by Warren et al. We find that the degree of cooling is not well correlated with the reported slopes of the emission measure distribution. We also conclude that the Fe XVIII emitting plasma that they measured is mostly in a state of cooling. These results support the idea that nanoflares have a distribution of energies and frequencies, with the average delay between successive events on an individual flux tube being comparable to the plasma cooling timescale.

Key words: methods: observational – Sun: atmosphere – Sun: corona – Sun: UV radiation

1. Introduction

Despite many decades of research, understanding how the solar corona reaches temperatures of greater than 1 MK while the photosphere below is only 6000 K remains one of the great unsolved problems of solar and space physics. There are many approaches to making progress on this difficult problem; one is to focus on physically distinct sub-regions of the solar corona, such as active regions (ARs), and isolated features within ARs, such as coronal loops. Since the magnetic field energy is so much larger than the plasma energy in the corona, every flux tube that is a part of a coronal feature (e.g., the bundle of flux tubes that comprise a coronal loop) can be modeled as an independent atmosphere.

ARs are locations of concentrated magnetic field, enhanced extreme ultra violet (EUV) and X-ray emissions, and generally are hotter than the quiet Sun corona surrounding them. Coronal loops within ARs are observationally defined by their enhanced brightness as compared to the diffuse emission surrounding them. The flux tubes comprising loops may undergo unique heating dynamics (e.g., an avalanche of nanoflares, Klimchuk 2006), or they may undergo the same heating dynamics as the diffuse emission, with “loops” appearing randomly as the result of the flux tubes that happen to be illuminated at a given time (e.g., Guarrasi et al. 2010). A standard approach for analyzing coronal loops is to examine their intensity as a function of time (light curves) in several EUV or X-ray channels, and it is usually found that loops are in a state of cooling (Winebarger & Warren 2005; Ugarte-Urra et al. 2006, 2009; Warren et al. 2007, 2010; Mulu-Moore et al. 2011b; Viall & Klimchuk 2011; Reale 2014). The loop is observable first in a hot (≥ 3 MK) channel, followed later in cooler channels. The peak emission is reached at successively later times in successively cooler channels. Based off of these and other observations, most researchers agree that loops are composed of many nanoflare-heated flux tubes,

each of which is unresolved with current coronal instrumentation (Cargill & Klimchuk 1997; Warren et al. 2002, 2003; Winebarger et al. 2003; Winebarger & Warren 2005; Klimchuk 2006, 2009, 2015; Patsourakos & Klimchuk 2008). This understanding has been confirmed by the ability of models of nanoflare-heated, subresolution flux tubes to reproduce the many different observables (Warren et al. 2002; Bradshaw & Cargill 2006, 2010; Klimchuk et al. 2008; Schmelz et al. 2014). Additionally, it was often assumed that loops undergo cooling to below the 171 Å channel peak sensitivity of 0.8 MK. For example, Warren et al. (2003) simulated loops as flux tubes cooling to as low as 0.1 MK. Prior to the launch of the *Solar Dynamics Observatory* (SDO), with its additional 131 Å channel sensitive to ~ 0.5 MK plasma, it was rare to find data with the sufficient temperature, spatial, and temporal coverage to follow the cooling of an observed ~ 1 MK loop to below 0.8 MK. With SDO, we are now able to statically test how often cooling from 0.8 to 0.5 MK occurs in loops and the diffuse emission.

We use the term “nanoflare” to mean an impulsive heating event, but do not ascribe a particular physical mechanism to it. Nanoflares are unresolved by current instrumentation, so all that is currently known is that the mechanism results in impulsive heat deposition. Furthermore, most proposed mechanisms, including wave heating, have the property that energy is deposited impulsively in elemental magnetic strands (Klimchuk 2006), therefore it is highly unlikely that coronal heating is ever truly steady. The important property is the frequency, or repeat time, of nanoflares on single flux tubes. Those flux tubes on which the average repeat time of the nanoflare is much longer than the plasma cooling time, as in the Parker paradigm (Parker 1988), are low frequency. High frequency nanoflares have repeat times that are very short relative to the plasma cooling time, and produce effectively

“steady” heating. Medium frequency nanoflares have repeat times that are of the order of the plasma cooling time.

An alternative possibility for explaining coronal loops is thermal non-equilibrium (Mok et al. 2008; Lionello et al. 2013; Mikić et al. 2013; Froment et al. 2015). In this scenario, the heating is effectively steady, and the heating is concentrated near the base of the corona. No equilibrium exists, and so the plasma undergoes heating and cooling cycles even though the energy release is steady. This usually involves the formation of a cold condensation, which falls down the loop leg. Winebarger et al. (2016) recently investigated the time lag signatures of an AR model in which the condensation process is aborted before cool temperatures are reached. Thermal non-equilibrium as an explanation for AR loops has not undergone the same thorough testing that nanoflare heating has. For example, observations show that coronal loop intensities are several times higher than that of hydrostatic equilibrium (Winebarger et al. 2003). This is difficult to explain with thermal non-equilibrium, since thermal non-equilibrium loops spend most of their time near to hydrostatic equilibrium prior to the rapid collapse of the condensation. Furthermore, Klimchuk et al. (2010) showed that simulations of thermal non-equilibrium do not reproduce all of the observed characteristics of coronal loops; however, those simulations were restricted to simplified geometries. N. M. Viall et al. (2017, in preparation) showed that thermal non-equilibrium where cool condensations form produce distinct time lag signatures that are different from those of Viall & Klimchuk (2012, 2013, 2015) and those that we will show here. The role of thermal non-equilibrium in such situations is being actively investigated at this time.

Though well-studied, coronal loops generally comprise only a small proportion of the AR emission. They are relatively weak (10%–30%) enhancements over the “background” (Del Zanna & Mason 2003; Viall & Klimchuk 2011). Therefore, an analysis approach that analyses all emission, including the diffuse emission surrounding coronal loops, is necessary. Recent investigations have analyzed the diffuse emission using the emission measure (EM) slopes of the diffuse emission in the cores of ARs. Models demonstrate that the slope α of the EM distribution coolward of the peak $EM(T) \propto T^\alpha$, is an indicator of how frequently the plasma is heated relative to a typical plasma cooling time (e.g., Mulu-Moore et al. 2011a; Warren et al. 2011; Bradshaw et al. 2012; Ugarte-Urra & Warren 2012; Reep et al. 2013). Several teams have attempted to measure the slope with data from the EIS spectrometer on Hinode (Tripathi et al. 2011; Warren et al. 2011, 2012; Winebarger et al. 2011; Schmelz & Pathak 2012) with varying results. One difficulty is the large uncertainty in the measured slopes (Guennou et al. 2013). Even accounting for this uncertainty, some AR cores have shallow slopes, consistent with low frequency nanoflares, while others have steeper EM slopes, seemingly more consistent with “steady heating,” or high frequency nanoflares (Warren et al. 2012). One limitation of EM slopes is that the measurements with the spectral resolution of EIS are not made over large spatial areas or continuously for long times, due to limited data.

A complementary approach to understanding both coronal loops and the diffuse emission between is to use the information contained in the light curves. This has been done previously on coronal loops, but applying it to the diffuse emission requires an automated, systematic analysis method, and modeling for understanding the optically thin contributions

from all of the flux tubes along the line of sight. Viall & Klimchuk (2012; henceforth VK12) developed a method for identifying plasma temperature dynamics in the entire AR, and showed how to interpret the measurements with forward modeling in a series of follow-on papers (Viall & Klimchuk 2013, 2015, 2016). For the first time ever, they used images from the Atmospheric Imaging Assembly (AIA; Lemen et al. 2011; Boerner et al. 2012) on board *SDO* and examined the light curves on a pixel-by-pixel basis of an entire AR using the time lag method. They found that the majority of coronal pixels (those in which the line of sight is not contaminated by bright transition region moss) contained plasma that was dynamic and undergoing cooling. Importantly, it was not only a few isolated locations associated with coronal loops that exhibited the cooling; rather it was the diffuse emission between loops as well. The time lag signal in the pixels dominated by transition region emission is also consistent with post-nanoflare cooling (Viall & Klimchuk 2015, 2016).

Warren et al. (2012; henceforth, WWB12) did a large scale study of 15 solar ARs, including NOAA AR 11082 studied by Viall & Klimchuk (2011, 2012). WWB12 chose this particular set of 15 due to their quiescent nature and the broad range of characteristics they exhibited. The set covered a large range of age, total unsigned magnetic flux, and area, and provides a good opportunity to test how nanoflare properties depend on various AR characteristics. They analyzed each AR with EIS data and measured the EM slope α , at a location in the core of the AR at a given time. They used *SDO*/AIA data to analyze the amount of hot, 7 MK plasma in the ARs.

For the 15 ARs, they found that NOAA AR 11082 did have a shallow slope, consistent with low frequency nanoflares and the VK12 results. However, they found that it had one of the shallowest slopes, with many of the other 14 ARs having steeper slopes that are difficult to explain with low frequency heating. This result called into question the universality of the cooling time lags observed in NOAA AR 11082. WWB12 also were able to isolate the hot, 7 MK contributions to the *SDO*/AIA 94 Å channel, which is a bimodal channel sensitive to both hot 7 MK plasma as well as warm 1 MK plasma. They show that ARs with higher unsigned magnetic flux had steeper EM slopes, more 7 MK plasma, and less lower temperature emission. They argue that the high temperature plasma in ARs is often close to equilibrium, which can only be explained by high frequency nanoflares or truly steady heating.

In this paper, we test whether the high temperature AR emission in all 15 ARs is indeed close to equilibrium, or if instead there is dynamic plasma behavior, with post-nanoflare cooling observed as in AR 11082. We compute time lag maps for the same 15 ARs, at the same times, as the WWB12 study and show that even those ARs that are strongly peaked around 4 MK and have steep EM slopes, have post-nanoflare cooling signatures as in AR 11082. Though these results may seem contradictory, we suggest a picture that reconciles the controversy and simultaneously explains all of these complementary observations using a recently proposed framework based on the idea that nanoflares have a distribution of sizes and frequencies, with the most common frequency being intermediate between low and high (Cargill 2014; Cargill et al. 2015; Lopez Fuentes & Klimchuk 2015, 2016; Bradshaw & Viall 2016). Additionally, our time lag test provides an independent method of identifying the presence of hot 7 MK

plasma in the 94 Å channel, which we find to be consistent with the WWB12 results.

2. Methods

We analyze 15 quiescent ARs observed by *SDO*/AIA. We chose the same 15 AR used in the WWB12 study. We apply our time lag method using data taken in six channels: 131, 171, 193, 211, 335, and 94 Å. The *SDO*/AIA data set is ideal for time lag analysis due to its continuous coverage, high spatial resolution, and rapid cadence. We use the full 12 s time resolution data, full 0".6 spatial resolution, and analyze 12 hr of continuous data for each AR, following VK12. Generally, we chose the 12 hr window such that it was centered on the time of the EIS analysis in WWB12. The time lag method, as with all time series analyses, is most accurate when the data are continuous and evenly sampled. Therefore, in a few cases, we chose a 12 hr interval that was not centered on (but still included) the time of the EIS analysis of WWB12 to avoid data gaps either due to spacecraft maneuvers or times of large flaring activity. We show an image of each of the 15 ARs in 171 Å in Figure 1. We overlay green boxes at the location where WWB12 performed their EIS analysis. We also list the 15 ARs, and the time interval of analysis, in Table 1. The ARs are all near to disk center, so derotation is straightforward, and projection effects are minimized. We derotate the 12 hr of data using differential rotation and accounting for fractional pixel rotation following VK2012.

For each AR, we apply the time lag method to the full 12 hr of data on a per-pixel basis. A full description of the method can be found in VK12 and we summarize here. At each pixel, we cross-correlate the emission in a given *SDO*/AIA channel as a function of time (i.e., a light curve) with the emission as a function of time in a different *SDO*/AIA channel. We test for correlations at different time lags by shifting the light curves both forward and backward in time relative to each other, up to two hours. At each pixel location, we record the time lag of maximum correlation and make maps of the results (shown in Figures 2 and 4). Using the six different *SDO*/AIA channels, we produce 15 different time lag maps.

Using the time lag convention set in VK12, we generally test the hotter channel first, and the cooler channel is moved forward and backward in time relative to the first (the exception are pairs with the bimodal channels 94 and 131 Å, which we describe later). The result of this convention is that positive time lags, i.e., when the second channel varies later in time than the first, indicates cooling. A cooling time lag is the result expected for low frequency nanoflare heating, where each flux tube cools after being impulsively heated. An important characteristic of impulsive heating is that the heating phase itself is essentially invisible. This is because the heating phase is short relative to the cooling time, and because the corona initially has lower density. It is only after the heat has conducted downward to the footpoints and chromospheric evaporation has taken place that the corona is dense enough to have bright emission. The post-nanoflare cooling phase is what dominates the emission, and that is the variability that the time lag method will identify when there are nanoflares present.

The positive time lags resulting from post-nanoflare cooling behavior are well understood and predicted for loops (Viall & Klimchuk 2011). Crucially, even in the diffuse emission where there are no identifiable loops, nanoflares still produce a positive time lag. Viall & Klimchuk (2013) showed that the

post-nanoflare cooling signal will dominate the time lags even in extreme cases with tens of thousands of flux tubes all along the line of sight, all undergoing nanoflares of different amplitudes and durations, all initiated at different, random times. This is because each nanoflare produces an intensity change and, even if it is relatively small, each one follows the same hot-to-cool progression through the channels. In every case, the cooling phase dominates the emission, since the cooling plasma is denser and the emission intensity scales as n^2 . Therefore, the composite of all of these small-scale intensity fluctuations still combine to yield a positive time lag with a large cross-correlation value. This is important because the predicted and observed variability of the diffuse emission is small relative to the mean intensity, and is difficult to distinguish from noise or random fluctuations without the time lag method.

In the other direction, negative time lags indicate that the variability in the second channel precedes that of the first. In our convention, this could indicate that the heating phase is brighter than the cooling phase and dominates the integrated emission—in other words, slowly increasing, quasi-steady heating. It could also indicate that there is more complex ensemble behavior, e.g., the nanoflares slowly increasing in intensity over a large area. Lastly, it can also be produced by plasma that is undergoing thermal non-equilibrium (Winebarger et al. 2016; N. M. Viall et al. 2017, in preparation). Despite all of these possible causes of negative time lags, they are rarely observed in the main body of the ARs of Viall & Klimchuk (2012, 2015) or those shown here.

The interpretation of positive and negative time lags is less straightforward in the case of pairs with the 94 Å channel. This is because the 94 Å channel is sensitive to plasma at both 7 MK due to a strong Fe XVIII line, as well as cooler plasma around 1 MK. In the convention set by VK12, we always test the 94 Å channel as the first channel as though it is a hot, 7 MK channel. For strong nanoflares, the channel is indeed dominated by hot emission and it peaks before any other AIA channel. However, for weaker nanoflares, the cooler emission dominates, and 94 Å peaks after 335, 211, and 193, but before 171 and 131 Å (Viall & Klimchuk 2011, 2012).

It is important to have several channel pairs to resolve ambiguity. For example, a negative time lag between 94 and 335 Å could be due either to impulsive heating by weak nanoflares or to a slow increase in quasi-steady heating, as described above. In the context of the five other channels, however, it is simple to make the distinction: in locations where there is post-nanoflare cooling indicated by positive time lags in channel pairs without 94 Å, a positive time lag with 94 Å indicates that hot 7 MK plasma dominates the emission variability, and a negative time lag indicates that cool 1 MK emission dominates the emission variability. This is a valuable discriminator between strong and weak nanoflares.

The 131 Å channel is also bimodal. Its primary sensitivity is to Fe VIII, at 0.5 MK, but it also has sensitivity to Fe XXI at 13 MK. This very hot plasma is typically only expected to be present in large quantities in large flares, and VK12 found no evidence of a hot contribution to 131 in their analysis of AR 11082. However, Viall & Klimchuk (2011) showed that, in principle, with a strong enough nanoflare, 131 could be dominated by hot plasma and, like 94, would exhibit post-nanoflare variability prior to all the other channels. In the present survey, several of the ARs show evidence of some hot

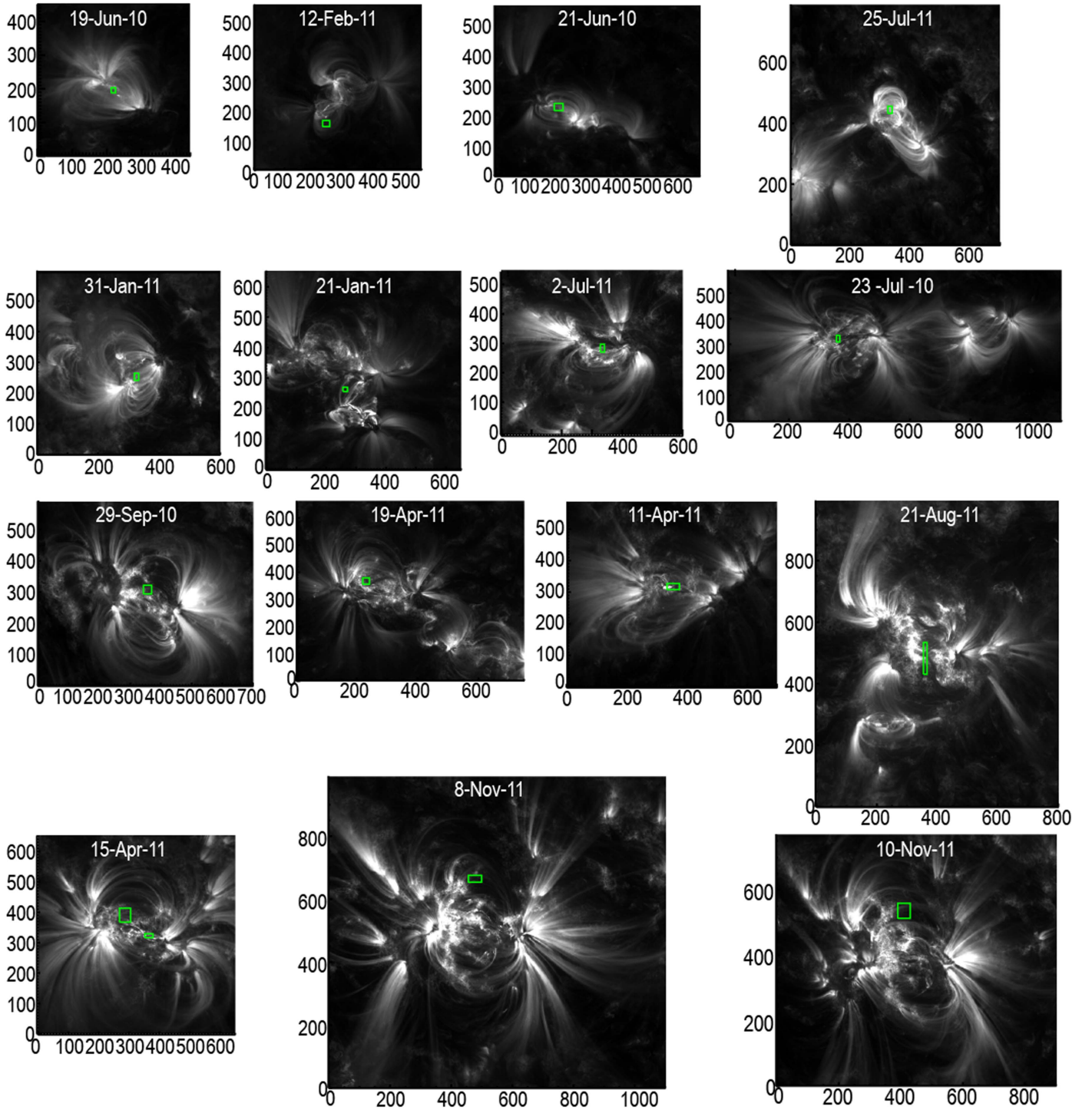


Figure 1. *SDO/AIA* observations in 171 Å of each of the active regions. Axis labels are in pixels. The green boxes indicate the region used by WWB2012 and for the time lag statistics in Table 2.

131 emission, though most of the AR plasma is still consistent with a cool 131 sensitivity. A full analysis is beyond the scope of this paper, and will be written up in a follow-on detailed analysis.

The third possible time lag result is a time lag of zero. This does not indicate a lack of variability, which is a common misconception. A time lag of zero indicates variability in both channels, but with no temporal offset between them (to within the 12 s resolution on the AIA instrument). In other words, the evolving emission is in phase in the two channels. The

transition region's response to a coronal nanoflare will produce precisely this behavior. If there is transmission region emission detected in two *SDO/AIA* channels, then the expected time lag is zero. As defined here, the transition region is the section of a coronal flux tube at the base where thermal conduction is a heating term (Vesecky et al. 1979). It reaches a temperature of roughly half the peak temperature in the tube, or several million Kelvin in the case of a nanoflare (Klimchuk et al. 2008). Viall & Klimchuk (2015) showed with analytical theory and numerical simulation that the transition region emissions seen

Table 1
ARs are Ordered in Increasing Total Unsigned Magnetic Flux, Following WWB2012

| NOAA AR | AR # | Date/Time Range | Positive 94–335 Å Time lag Pixels $\times 10^4$ | Fe XVIII Flux, WWB2012 |
|---------|------|----------------------------|---|------------------------|
| 1082 | 1 | 2010 Jun 19 00:00-12:00 | 2.8 | 1.36(04) |
| 1158 | 2 | 2011 Feb 12 12:00-24:00 | 2.9 | 1.88(04) |
| 1082 | 3 | 2010 Jun 21–22 20:00-08:00 | 2.4 | 1.05(04) |
| 1259 | 4 | 2011 Jul 25 03:00-15:00 | 4.8 | 7.81(03) |
| 1150 | 5 | 2011 Jan 31 00:00-12:00 | 4.7 | 1.47(05) |
| 1147 | 6 | 2011 Jan 21 08:00-20:00 | 9.7 | 2.28(05) |
| 1243 | 7 | 2011 Jul 02 00:00-12:00 | 4.1 | 6.18(04) |
| 1089 | 8 | 2010 Jul 23 12:00-24:00 | 5.1 | 1.84(05) |
| 1109 | 9 | 2010 Sep 29–30 13:00-01:00 | 4.6 | 1.50(05) |
| 1193 | 10 | 2011 Apr 19 07:00-19:00 | 6.6 | 2.50(05) |
| 1190 | 11 | 2011 Apr 11 03:00-15:00 | 6.7 | 1.11(05) |
| 1271 | 12 | 2011 Aug 21 06:00-18:00 | 7.8 | 1.47(05) |
| 1190 | 13 | 2011 Apr 15 00:00-12:00 | 8.9 | 5.22(05) |
| 1339 | 14 | 2011 Nov 8 08:00-20:00 | 21.8 | 6.08(05) |
| 1339 | 15 | 2011 Nov 10 02:00-14:00 | 15.8 | 9.75(05) |

Note. Fourth column lists the number of positive time lag pixels measured for the entire AR in the 94–335 Å pair with a cross-correlation value higher than 0.2. Fe XVIII flux is the total intensity per WWB2012.

in all six *SDO*/AIA channels should have zero or near-zero temporal offset during post-nanoflare cooling. They also presented two observational arguments supporting the interpretation that the zero time lags observed in ARs are due to the transition region response to coronal nanoflares. First, they computed time lags in an AR observed over the limb, where the pixels imaging the AR do not observe transition region plasma. They found that the amount of near-zero time lags dropped dramatically as compared to the **VK12** AR, which was observed on-disk where many pixels simultaneously measure transition region and coronal plasma. Second, they found that the zero time lags in **VK12** were correlated with locations of moss and regions of high magnetic field concentration, where coronal flux tubes would be rooted, and where the transition region would be. Lastly, Bradshaw & Viall (2016) confirmed that zero time lag will occur in the footpoints for all AIA channel pairs in their AR modeled with nanoflare heating.

Bradshaw & Viall (2016) also showed that zero time lag can occur in the corona in the case of medium frequency heating. This is due to a combination of two things. First, the AIA response functions are fairly broad for all of the channels, with significant overlap in temperature sensitivity for all six channels. Second, in a medium frequency, by definition, the plasma cools only partially before being reheated. In other words, it cools into but not through the range of sensitivity of both passbands, which produces variable coronal emission with no temporal offset.

Importantly, zero time lag is inconsistent with steady emission from steady heating. Steady emission has no variability, by definition. The key to the time lag method is that it cross-correlates variability. Strongly correlated signals indicate time variable emission. In the case of steady emission, the variability that the cross-correlation identifies is due entirely to noise. Though it will still find a peak cross-correlation value, it will be very low (less than 0.03, Viall & Klimchuk 2013, 2016), and it will randomly occur at any of the tested time lag values with equal likelihood of identifying positive and negative time lags (Viall & Klimchuk 2016). A time lag of zero would be rarely identified. Finally, physically connected structures arise independently in our time lag maps, even though we construct the time lag maps on a pixel-by-pixel

basis. This coherence cannot be due to noise and indicates physically variable phenomena occurring on the Sun.

3. Results

For each of the 15 ARs, we compute maps of the measured time lags for each channel pair. With six different channels in *SDO*/AIA, there are 15 different channel pairs. We show the results from five representative pairs in Figures 2(a)–(e): 94–335, 94–171, 335–211, 335–171, and 193–171 Å, for each of the 15 ARs. Each column displays all of the results from a single AR, and each row shows the results for a given channel pair. Figure 2(a) shows the first four ARs, 2(b) shows the second four ARs, 2(c) shows the third four ARs, and 2(d) shows the final three ARs. Following WWB12, the ARs are ordered according to increasing unsigned magnetic flux in Figures 1, 2, and 4 and both tables. The channel pairs that we used for Figure 2 are representative in that they span almost the full and relevant range of AIA temperature sensitivity, from 0.8 MK (171 Å) through 2.5 MK (335 Å) and up to 7 MK (94 Å). Reds, oranges, and yellows indicate positive time lags, or cooling, likely in the aftermath of a nanoflare. Blues, greens, and blacks, though rarely present, indicate negative time lags. Olive green indicates zero or near-zero time lag. In Figure 4, we show maps of the coolest channel pair, 171–131 Å for all 15 ARs, showing evolution from 0.8 MK to 0.5 MK, and we discuss those results in further detail later.

The first result seen in Figure 2 is that there is widespread cooling, indicated by many positive time lags in all of the channel pairs (with the exception of 94–335 Å, due to the bimodal 94 nature). The result holds for all 15 ARs. Note, in particular, that it is not just a few isolated coronal loops that exhibit cooling, but rather the entire core of the AR, including the diffuse emission surrounding loops. The fact that patterns in the time lag maps follow the magnetic field topology, which is suggestive of coherence along magnetic field lines, provides additional confidence in the cooling interpretation. The other feature that dominates the maps is a large presence of zero time lags. As predicted by the models (Viall & Klimchuk 2015; Bradshaw & Viall 2016), this is expected in the transition region, and generally, the zero time lags are indeed concentrated at the flux tube footpoints (though see the later discussion of Table 2

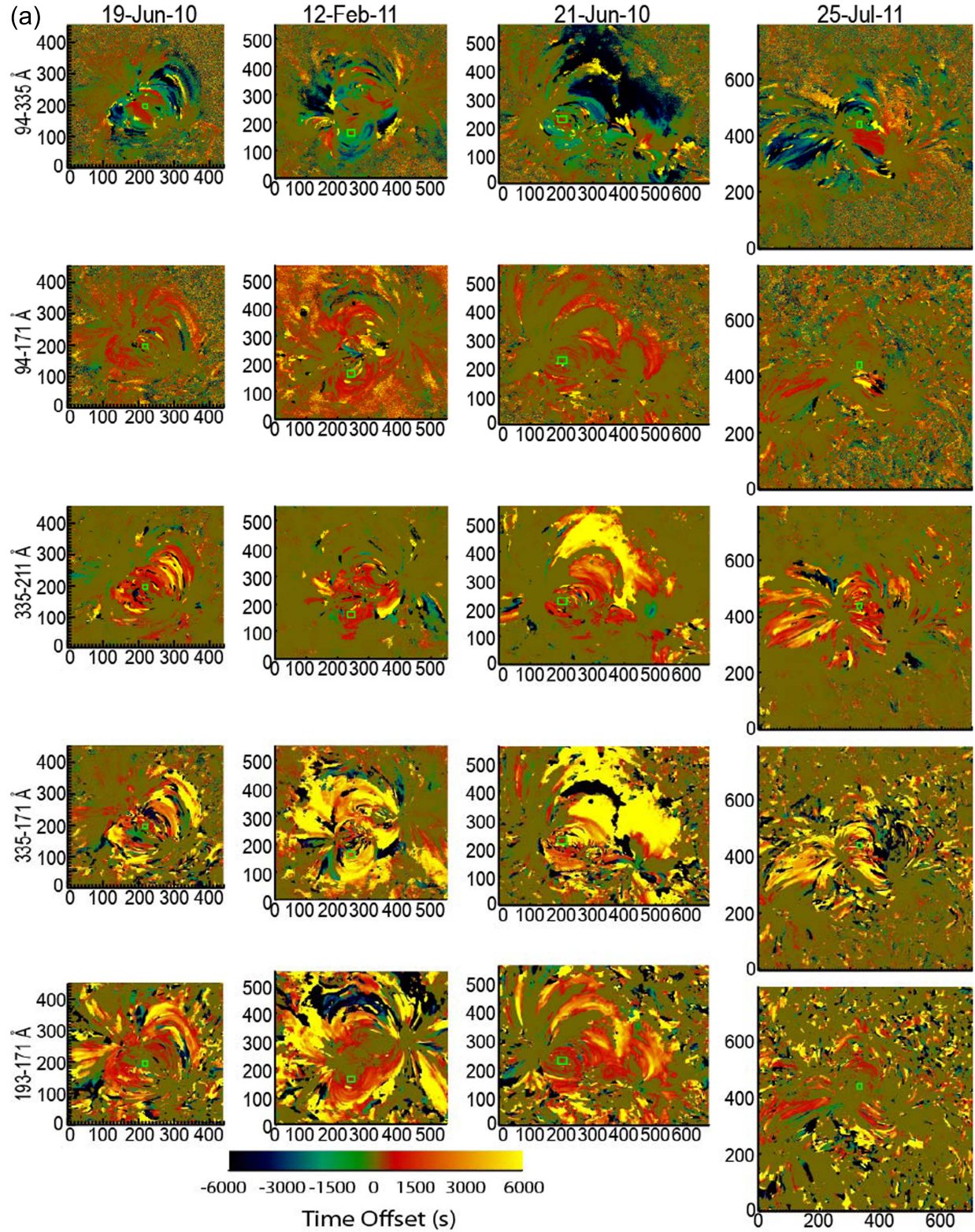


Figure 2. Time lag maps computed between different *SDO*/*AIA* channel pairs (listed to the left) for five representative channel pairs for all 15 AR. Color bar is identical in all time lag maps. (a) shows the first four ARs, (b) shows the second four ARs, (c) shows the third four ARs, and (d) shows the final three ARs.

results showing zero time lags observed occasionally in the corona too, and also see the discussion of Figure 4 and the 171–131 Å pair where the majority of the corona also exhibits zero time lags). There is very little presence of negative time lags in any of the ARs. We conclude that there is variable emission consistent with post-nanoflare cooling in the vast majority of

pixels for all ARs. This result holds for all of the ARs, regardless of their EM slopes.

The results in the 94–335 Å pair are also consistent with post-nanoflare cooling. In all 15 ARs there is evidence that the hot, Fe XVIII, 7 MK plasma dominates the 94 Å emission in at least part of the AR. This is generally in the core, where the

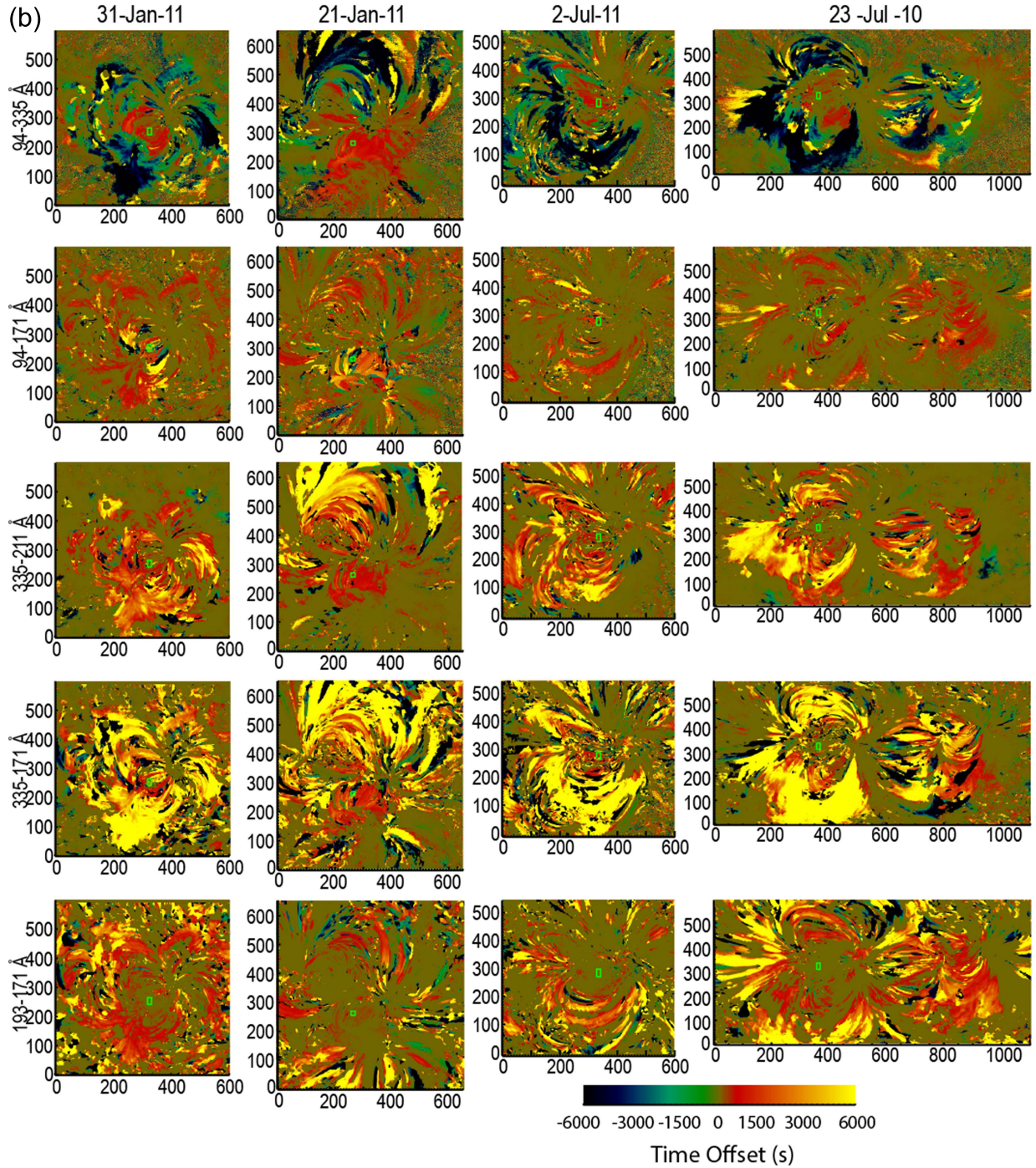


Figure 2. (Continued.)

magnetic field is stronger and nanoflares are expected to be more energetic. Focusing on the main body of the AR (i.e., not the fan loops on the periphery, or quiet Sun surrounding the AR), widespread cooling is indicated by the other channel pairs. Given this fact and the discussion in the Methods section, a positive time lag in the 94–335 Å pair means that 7 MK plasma dominates the 94 Å emission, and a negative time lag means that cooler, 1 MK plasma dominates the emission. As in the other channels, zero time lag in moss regions occurs in all of the maps.

In Table 1, we compute the total number of pixels (proportional to the area, where the constant of proportionality

is the pixel area) that contain positive time lags in the 94–335 Å pair with a cross-correlation value of 0.2 or greater. We found in VK2012 that the cross-correlation value was dependent on the count rates, and channel pairs with higher count rates statistically had higher cross-correlation values. This is expected because higher count rates produce higher signal-to-noise ratios, and so the relative variability due to noise fluctuations is reduced with higher count rates. VK2012 found that for the 94–335 Å pair, omitting time lags with a cross-correlation value lower than 0.2 safely excluded the AR periphery and areas of low count rates, while retaining the AR core. Note that even though 0.2 is not exceptionally high, it is

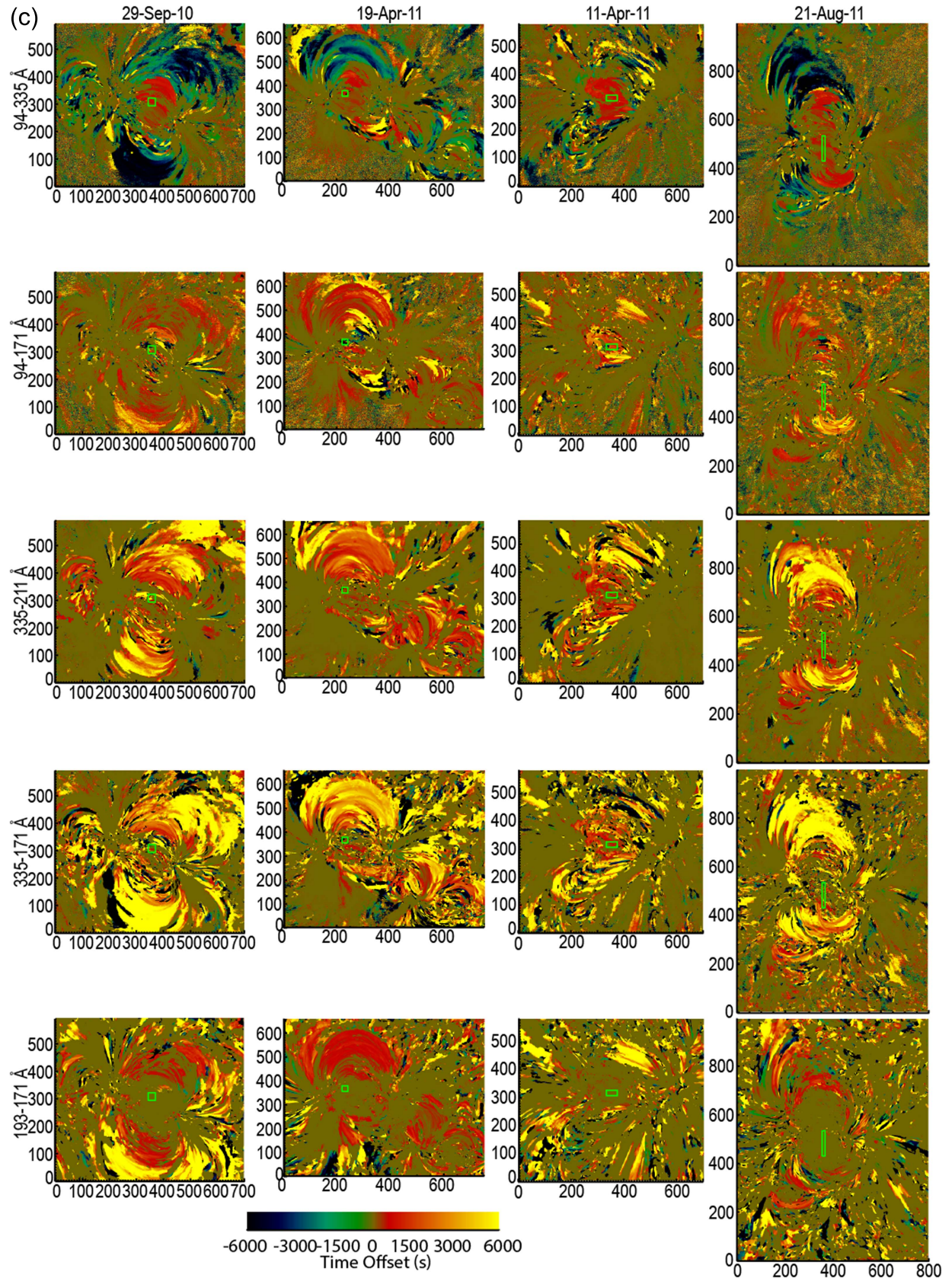


Figure 2. (Continued.)

much greater than the 0.03 expected from Poisson noise. In summary, the number of pixels listed in Table 1 is directly related to the area in the AR cores where 94 \AA emission is

dominated by 7 MK plasma, and that plasma is cooling from 7 MK down to at least 2.5 MK (the 335 \AA peak temperature sensitivity).

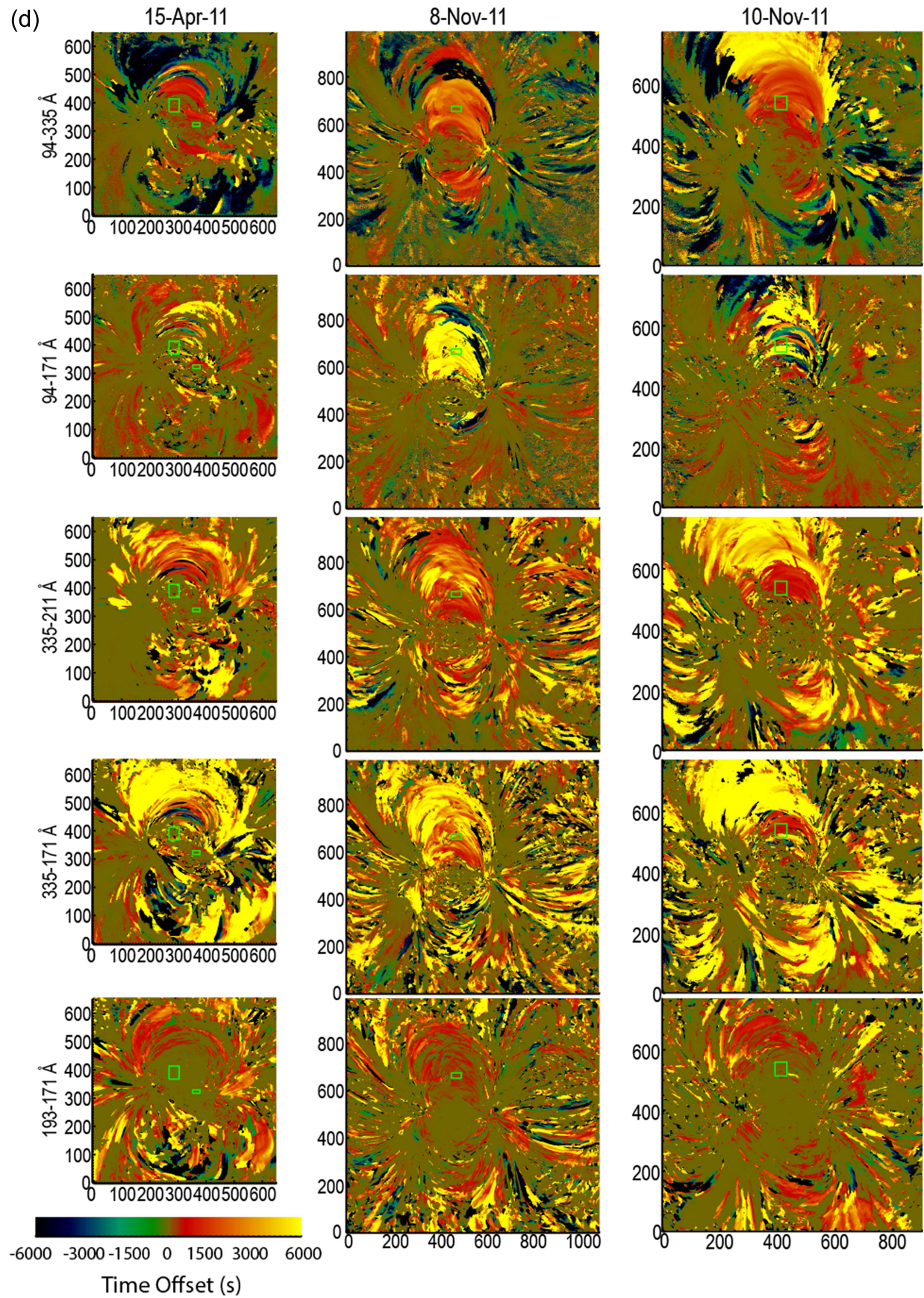


Figure 2. (Continued.)

Table 2
 α is the Slope of the Emission Measure Distribution from Log T 6.0 to 6.6 per WWB2012 Measured with EIS in a Small Subfield of the AR

| NOAA AR | AR # | α | 94–335 Å | 335–211 Å | 193–171 Å | 171–131 Å |
|---------|------|----------|-----------------------|-----------------------|-----------------------|-----------------------|
| | | | %pos %zero %neg | %pos %zero %neg | %pos %zero %neg | %pos %zero %neg |
| 1082 | 1 | 2.2 | 100% | 100% | ... | ... |
| | | | ... | ... | 100% | 100% |
| | | | ... | ... | ... | ... |
| 1158 | 2 | 2.7 | 100% | 100% | 100% | ... |
| | | | ... | ... | ... | 100% |
| | | | ... | ... | ... | ... |
| 1082 | 3 | 2.0 | 35% | 58% | 100% | 1% |
| | | | 50% | 41% | ... | 99% |
| | | | 15% | 1% | ... | ... |
| 1259 | 4 | 2.0 | 25% | 71% | 3% | ... |
| | | | 54% | 15% | 92% | 100% |
| | | | 21% | 14% | 5% | ... |
| 1150 | 5 | 2.2 | 96% | 31% | 1% | 1% |
| | | | 4% | 66% | 99% | 98% |
| | | | ... | 3% | ... | 1% |
| 1147 | 6 | 3.6 | 100% | 100% | 100% | 96% |
| | | | ... | ... | ... | 4% |
| | | | ... | ... | ... | ... |
| 1243 | 7 | 2.9 | 63% | 55% | ... | ... |
| | | | 35% | 45% | 100% | 100% |
| | | | 2% | ... | ... | ... |
| 1089 | 8 | 3.5 | 87% | 4% | ... | ... |
| | | | 13% | 91% | 100% | 100% |
| | | | ... | 5% | ... | ... |
| 1109 | 9 | 4.3 | 88% | 48% | ... | ... |
| | | | 12% | 49% | 100% | 100% |
| | | | ... | 3% | ... | ... |
| 1193 | 10 | 3.3 | 82% | 53% | 3% | ... |
| | | | 17% | 43% | 96% | 100% |
| | | | 1% | 4% | 1% | ... |
| 1190 | 11 | 3.0 | 96% | 67% | 37% | 4% |
| | | | 4% | 33% | 67% | 52% |
| | | | ... | ... | ... | 44% |
| 1271 | 12 | 3.6 | 79% | 48% | 2% | 1% |
| | | | 21% | 45% | 98% | 83% |
| | | | ... | 7% | ... | 16% |
| 1190 | 13 | 3.7, | 91%, 99% | 19%, 85% | ..., 14% | 4%, 1% |
| | | 3.3 | 9%, 1% | 75%, 15% | 100%, 86% | 77%, 34% |
| | | ... | ... | 6%, ... | ..., ... | 19%, 65% |
| 1339 | 14 | 4.8 | 100% | 89% | 87% | 1% |
| | | | ... | 3% | 12% | 1% |
| | | | ... | 8% | 1% | 98% |
| 1339 | 15 | 3.7 | 100% | 100% | 75% | 7% |
| | | | ... | ... | 23% | 60% |
| | | | ... | ... | 2% | 33% |

Note. In the right four columns, we list the percent of positive, zero, and negative time lags in those same subfields for four representative time lag pairs, with decreasing temperature from left to right.

We compare this with the total (spatially integrated) intensity of Fe XVIII in the same AR cores, as measured by WWB12. They isolated the Fe XVIII emission in the AIA 94 Å channel by subtracting the cooler contribution using the 171 and 193 Å channels. Figure 3 shows the total Fe XVIII emission from WWB12 plotted against the number of pixels with positive 94–335 Å time lag. There is a strong positive correlation. This is clear evidence that the hot 7 MK plasma is cooling and not maintained in an equilibrium state by steady heating. This is consistent with the dynamic fluctuations of Fe XVIII emission found by Ugarte-Urra & Warren (2014). It is possible that not

all of the 7 MK plasma is cooling, and the relative amounts of cooling and equilibrium plasma has yet to be determined.

In Figure 4, we show the results from the single channel pair 171–131 Å for all 15 ARs. This shows plasma variability between ~0.8 MK and 0.5 MK (the peak temperature sensitivities of 171 and 131 Å, respectively), and is the coolest channel pair that we analyze. These maps are in stark contrast to the maps shown in Figure 2: all 15 AR maps are dominated by zero time lags, even in the core of the AR, away from the moss. Though there are some post-nanoflare cooling signatures, easiest to see in the second and thirteenth ARs (2011 February 12 and

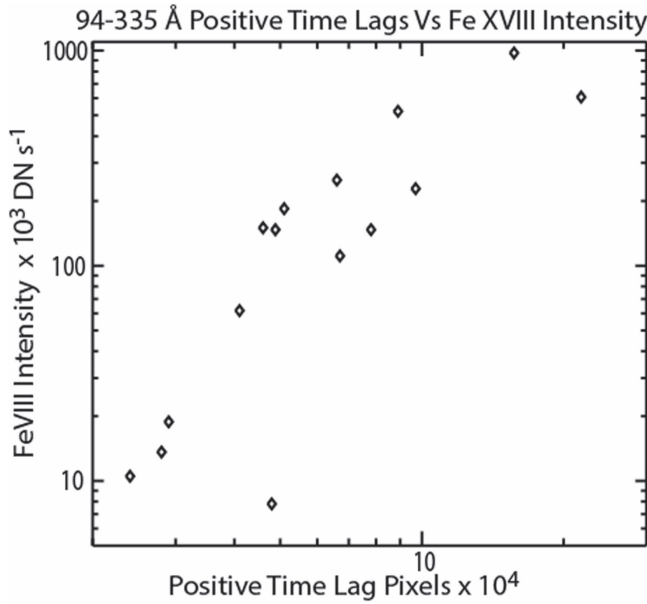


Figure 3. Number of positive time lags measured with greater than a 0.2 cross-correlation value in the 94–335 Å time lag maps vs. the amount of hot, Fe XVIII emission measured by WWB2012 for the same 15 ARs. Values taken from Table 1.

2011 April 15), in this channel pair they are in isolated loop features, rather than also the diffuse emission throughout the AR. The presence of zero time lags in the core of the AR where all of the other channel pairs indicate cooling is consistent with plasma that is cooling into, but not through, the range of overlapping temperature sensitivity of the 171 and 131 Å channels (Bradshaw & Viall 2016). Note that there is significant overlap in the temperature sensitivities of the different AIA channels. So, for example, the 131 Å channel will still be sensitive to plasma that cools to 0.8 MK (where 171 Å peak sensitivity is) and reheats before reaching 0.5 MK. Taken with Figure 2, we conclude that the plasma in the corona often cools from 2.5 MK, and sometimes as high as 7 MK, down to 0.8 MK, but it rarely cools all the way to 0.5 MK. This is evidence for “medium frequency” nanoflares, where the repeat time is of the order of a cooling time (Bradshaw & Viall 2016). In a scenario of nanoflares, it makes sense that the reheating would occur somewhere between 2.5 and 0.8 MK from a statistical standpoint because the plasma spends more time between 2.5 and 0.8 MK than it does cooling from 0.8 down to 0.5 MK (e.g., Bradshaw & Cargill 2010).

Bradshaw & Viall (2016) found that for low frequency nanoflares, where the nanoflare repeat time is longer than 10,000 s, the plasma cools fully, resulting in positive time lags in the 171–131 Å channel pair in the corona. However, as the average nanoflare frequency increases (repeat times become shorter), the cooling phase is truncated just before full cooling, and the time lag maps show zero time lags even in the core of the AR, with only a few isolated loops exhibiting full cooling. Aborted condensations in the thermal non-equilibrium scenario may also produce partial cooling behavior (Winebarger et al. 2016).

The final property of note in the 171–131 Å time lag maps is the lack of significant negative time lags. Those that do occur at the location of Fe XVIII emission could indicate the presence of even hotter, >10 MK, plasma, since the 131 Å channel also has sensitivity to such very hot emission. The most obvious

examples are the last two ARs (e.g., pixels around $x = 500$ and $y = 600$, 2011 November 8 and 2011 November 10). These ARs have the most unsigned magnetic flux of any in the set and might be expected to have the strongest nanoflares. Confirming the presence of >10 MK plasma requires a thorough investigation, which will take place in a follow-on paper.

Next, we compare our time lag results to the EM slopes measured in small sub-regions by WWB12 using EIS data. It is clear in looking at the time lag maps that small areas in the AR can behave differently than the statistical average. Furthermore, even though cooling patterns essentially permeate the whole AR for all 15 cases, the values of the time lags and whether or not hot, variable Fe XVIII emission exists are both highly dependent on location within the AR. This suggests that the small areas over which WWB12 measured the EM slopes may not always capture the typical AR behavior. It is nonetheless highly instructive to investigate the properties of the plasma in these sub-regions. WWB12 selected the small box-shaped regions to contain appreciable Fe XVIII emission and to avoid moss as much as possible. They are in the cores of the ARs. The boxes we use are meant to coincide with those in WWB12, but may not match exactly. We center the box on the EIS location listed in Table 1 of WWB12, and we approximate the dimensions by eye based on their Figure 1. Our boxes are over plotted on the images in Figure 1 and the time lag maps in Figures 2 and 4 in green. The boxes have a minimum of 10×10 AIA pixels, but many are bigger. In Table 2, we list the percentage of pixels in each box that contain positive, zero, or negative time lags for four representative channel pairs (94–335, 335–211, 193–171, and 171–131 Å), in decreasing temperature sensitivity. We also list the EM slope coolward of the peak, α , as measured by WWB12.

The first thing to notice from Table 2 is the overwhelming predominance of positive time lags in the 94–335 Å channel pair. Percentages approach or equal 100% for most boxes. Since all of the boxes contain appreciable Fe XVIII emission according to WWB12, we conclude that the 94 Å channel is mostly dominated by hot emission, and that the positive time lags indicate plasma cooling from 7 MK down to at least 2.5 MK. The two boxes without a predominance of positive lags (ARs 3 and 4) are from the two ARs with the weakest Fe XVIII emission. It is likely that cool emission dominates the 94 Å channel for many of the pixels in the boxes in these ARs.

The second thing to notice from the table is that the percentage of positive time lags decreases systematically in progressing from hotter to cooler channel pairs for each box. More precisely, with the exception of the aforementioned ARs 3 and 4, the percentage decreases or stays the same in going from 94–335 Å to 335–211 Å to 193–171 Å to 171–131 Å. In AR 11, for example, the percentage of positive time lags decreases from 96% to 67% to 37% to 4%. The positive time lags in these channel pairs correspond to cooling plasma in the approximate intervals 7–2.5 MK, 2.5–2.0 MK, 1.5–0.8 MK, and 0.8–0.5 MK, respectively. We conclude from this systematic behavior that the degree of cooling varies within the box. Some pixels (4%) are dominated by full cooling from >7 MK all the way down to <0.5 MK. Other pixels are dominated by partial cooling that reaches 0.8 MK ($33\% = 37\% - 4\%$), 2.0 MK ($30\% = 67\% - 37\%$), or 2.5 MK ($29\% = 96\% - 67\%$) before the next nanoflare reheats the plasma. This is fully consistent with there being a distribution of nanoflare

171-131Å Time Lag Maps

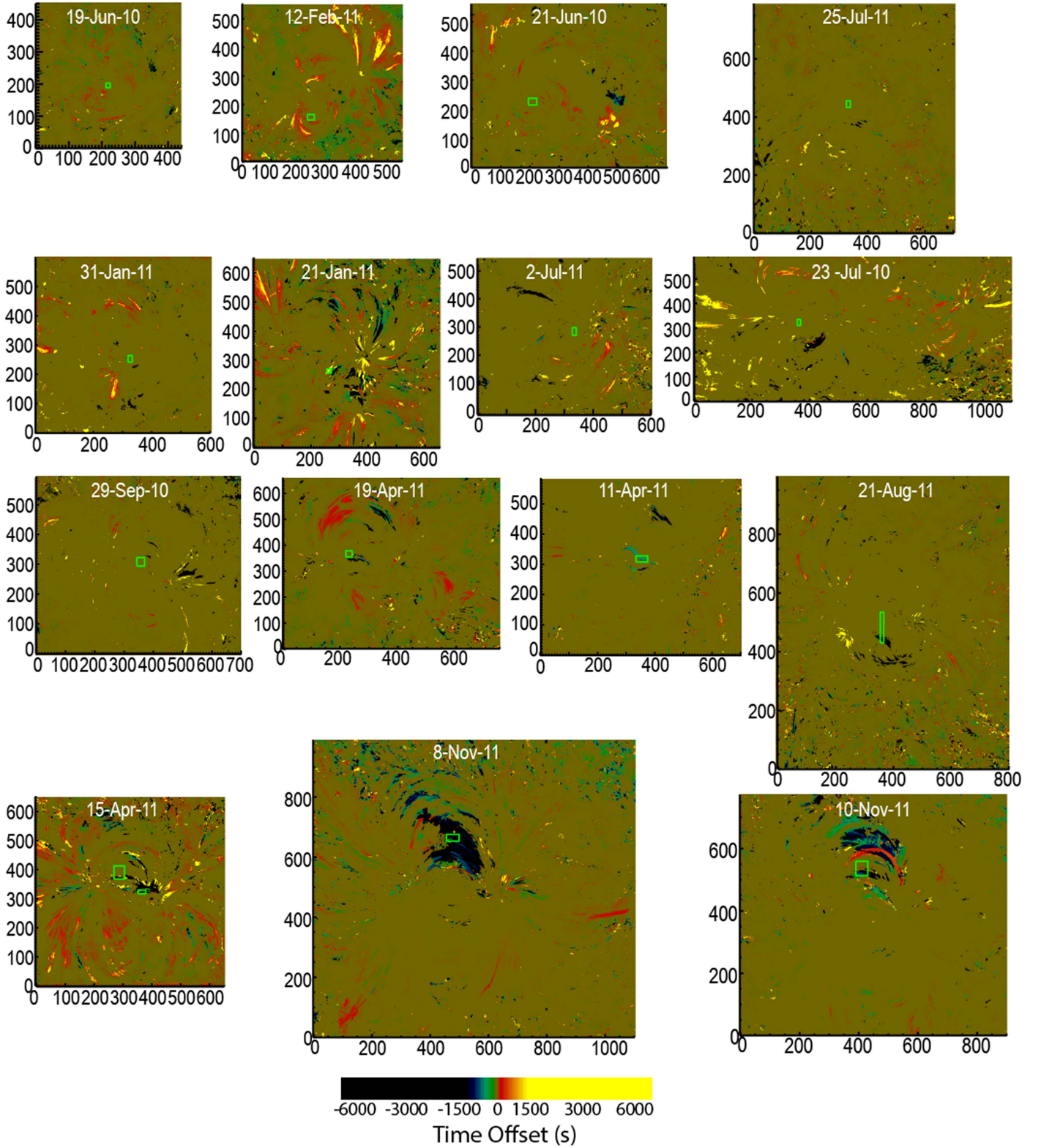


Figure 4. Time lag maps computed between the 171 and 131Å channel pair for all 15 ARs. Color bar is identical in all time lag maps, but is contracted relative to Figure 2.

frequencies, with the characteristic frequency of the order of an inverse cooling time, as proposed by Cargill (2014).

A different example is AR 2, where there are 100% positive time lags in the two hottest channel pairs and 0% positive lags

in the two coolest pairs. This suggests a more homogeneous situation where all the pixels are dominated by cooling from >7 MK to 2 MK. An example where there is some homogeneity, but not completely, is AR 15. There, the percentage of

positive time lags progresses from 100% in both of the two hottest channel pairs to 75% between 193–171 Å to 7% between 171–131 Å, indicating that, for three-quarters of the pixels, the dominant cooling goes all the way down to 0.8 MK.

The high percentage of zero time lags in 193–171 and 171–131 Å is predicted for AR heating where there is a distribution of medium frequency nanoflares (Bradshaw & Viall 2016). It is also possible that, although WWB12 attempted to avoid bright moss (footpoints of very hot loops) when choosing their boxes, some portion of the box includes 0.5–1.5 MK transition region emission from the lower legs of modestly hot loops. This is because temperature gradients in the upper part of the transition region can be shallow, and the transition region occupies nearly 10% of the loop leg (Klimchuk et al. 2008). In an inclined loop, this lower section of the leg could fall within the box even if the footpoint does not.

Finally, we note that only a very small percentage of pixels have negative time lags. The only exceptions are the 171–131 Å time lags in ARs 11, 13, 14, and 15. Since all of the boxes at these locations indicate cooling in the other channel pairs, and these ARs have high Fe XVIII total intensities, we speculate that the 131 Å channel may be dominated by emission in excess of 10 MK in these boxes. Recall that the 131 Å channel is bimodal with a peak at 13 MK. A highly correlated negative time lag would indicate plasma that has cooled from these extreme temperatures. Full cooling down to the 171 channel (0.8 MK) would not be surprising, since a very large amount of energy would need to be extracted from the magnetic field to power the nanoflare, and it is unlikely that another nanoflare would occur shortly thereafter (Klimchuk 2015). In addition, a stronger nanoflare will produce a relatively denser corona, which leads to faster cooling, and less time for a subsequent nanoflare to occur before the plasma has cooled.

As discussed earlier, the slope of the EM distribution has been thought to be a good indicator of nanoflare frequency. Shallow slopes indicate low frequency nanoflares where there is full cooling, and steep slopes indicate high frequency nanoflares where there is only partial cooling. We might therefore expect an inverse correlation between the slope and the percentage of positive time lags in the cooler channel pairs. However, we find no evidence for such a correlation. In Figure 5, we plot the percentage of positive time lags measured in the 193–171 Å channel pair for each AR box as a function of EM slope α , and show that there is no correlation. We interpret this apparent discrepancy as being due to the non-uniformity of nanoflares. The dependence of EM slope on nanoflare frequency is very clear when nanoflares are homogeneous (have a single magnitude and frequency). The dependence is more complicated when there are broad distributions of magnitude and frequency. We suggest that the slope and time lag results are fully consistent with each other and, together, are a powerful tool to infer what the distributions are. This will involve modeling and is something we plan for in the near future.

4. Discussion

It was important to confirm that full and partial cooling signatures occur in the precise locations where the EM distributions were measured in order to directly test any relationship between time lag signatures and EM slopes. As the disparity between the EM slopes measured at two different

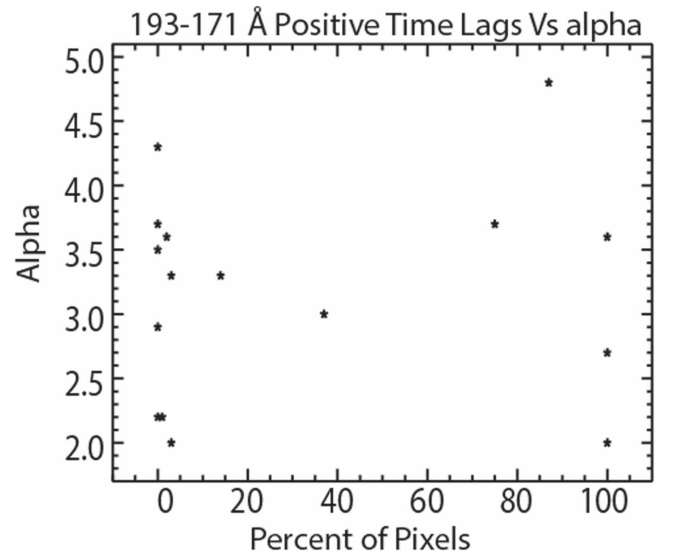


Figure 5. Percent of positive time lags measured in the 193–171 Å channel pair for each AR box as a function of EM slope α (from WWB2012). Values are listed in Table 2.

locations in AR 13 suggests, the EM slope is variable within an AR core. The degree of spatial variability in the time lag values is consistent with this too. Note that in some cases, the time lags measured adjacent to the box are different than those in the box. For example, the 94–335 Å box for AR 2 had 100% positive time lags, which is evidence for cooling from Fe XVIII, but there is a very large area immediately below the box that has negative time lags where 94 Å emission is dominated by cooler emission. AR 4, which was the AR with the smallest percentage (25%) of positive 94–335 Å time lags in the box, is another example. Immediately below the box is a very large area of positive time lag indicative of Fe XVIII emission cooling down into the 335 Å passband.

The spatial variability could indicate that nanoflare frequency is locally homogeneous, with different frequencies occurring in different parts of the AR; or there could be a distribution of frequencies everywhere (Cargill 2014) with different parts of the distribution dominating along different lines of sight. This highlights that while EM information is important, with our current instrumentation, it is incomplete, and therefore is highly complemented by these time lag maps. With our time lag maps, we capture the global picture and the range of activity occurring in the AR.

There is one important caveat to our claim of widespread cooling. Most lines of sight show evidence of fully or partially cooling plasma, but in addition to this cooling plasma, there could also be a component of steady plasma along the same line of sight. If this were a minor component, then it would not affect the measured time lag values. If steady emission dominates, however, then variations in the light curves would be controlled by photon noise and would be uncorrelated between the two channels (Viall & Klimchuk 2016). The time lag maps would exhibit random values (colors), and the cross-correlation values would be small. Neither is observed to be the case in any of the channel pairs, so we can state with confidence that steady plasma, though possibly present, does not dominate most lines of sight through any of the ARs presented in this study.

5. Conclusion

We compute time lag maps for 15 ARs between the six different *SDO*/AIA EUV channels. The ARs span a range of magnetic complexities, total unsigned magnetic fluxes, amount of hot (~ 7 MK) Fe XVIII emitting plasma, and measured EM slopes. Our time lag maps conclusively show that plasma cooling is occurring throughout the main body of every AR, even in places where the EM slope is steep. The observations are consistent with nanoflare heating. Whether they are consistent with other interpretations, such as aborted condensations associated with thermal non-equilibrium, has yet to be fully evaluated. It is important to note that the cooling plasma is present both in observationally distinct loops and in the diffuse component that surrounds loops. Areas of moss, which demarcate the transition region footpoints of hot coronal flux tubes, are dominated by time lags of zero. Such time lags are consistent with nanoflares (Viall & Klimchuk 2015; Bradshaw & Viall 2016), but not with steady plasma (Viall & Klimchuk 2016). Time lags of zero are also seen away from the moss in the core of the ARs, especially in cooler channel pairs with overlapping temperature sensitivity, and are indicative of partially cooling coronal plasma, where reheating occurs before lower temperatures are reached. A preponderance of zero time lags in 171–131 Å maps indicate that plasma only infrequently cools below ~ 0.8 MK. Given that time lags of ~ 3000 – 6000 s are typically observed between 335 and 171 Å, with little observed further cooling, we conclude that it is rare for the nanoflare repeat time to be much longer than ~ 5000 s.

We find clear evidence in all 15 ARs for hot (~ 7 MK) Fe XVIII emitting plasma cooling to at least 2.5 MK (335 Å channel) and often below. A good correlation between the number of pixels exhibiting such cooling and the amount of Fe XVIII emission reported by WWB12 suggests that most of the hot plasma is not in a steady state. Negative time lags in 171–131 Å maps provide evidence of even hotter (>10 MK) cooling plasma in some places. The hot and very hot plasma occur preferentially in the AR cores and in ARs with greater unsigned magnetic flux. This is where the magnetic field is expected to be stronger and nanoflares are expected to be more energetic.

Any viable theory of coronal heating must reconcile (1) the range of observed EM slopes, (2) the observed time lags, (3) the observed hot Fe XVIII emission, which is often—and probably usually—in a state of cooling, and (4) the observed truncated, partial cooling. There is a wide range of behavior exhibited by these ARs, and neither fully steady heating, nor low frequency nanoflares is an adequate explanation, even for individual ARs. We believe that one possible solution is nanoflares with a distribution of frequencies, where the wait time between events is sometimes long, and sometimes short. This would explain the observed varying degrees of cooling. Only occasionally is there full cooling from at least 7 MK, down through 0.5 MK. Cargill (2014) suggested that there is a distribution of nanoflare energies and wait times, and that the wait times and energies are linked, with the most common wait time being comparable to the plasma cooling timescale (i.e., medium frequency nanoflares). This seems to be a promising way to reproduce the full range of observed EM slopes (Cargill 2014; Cargill et al. 2015; Barnes et al. 2016; Lopez Fuentes & Klimchuk 2016) and the time lag results (VK2012; Bradshaw & Viall 2016) simultaneously. A key component to this idea is that along a given LOS, and over the course of the observing window, there will be magnetic flux

tubes undergoing both longer than average and shorter than average wait times.

We thank the reviewer for the thoughtful evaluation of this paper. This work was supported by the Heliophysics Guest Investigator Program. The data are courtesy of NASA/*SDO* and the AIA science team. This work benefited greatly from the International Space Science Institute team meeting “Coronal Heating—Using Observables to Settle the Question of Steady versus Impulsive Heating” led by Stephen Bradshaw and Helen Mason.

References

- Barnes, W. T., Cargill, P. J., & Bradshaw, S. J. 2016, *ApJ*, 833, 217
 Boerner, P., Edwards, C., Lemen, J., et al. 2012, *SoPh*, 275, 41
 Bradshaw, S. J., & Cargill, P. J. 2006, *A&A*, 458, 987
 Bradshaw, S. J., & Cargill, P. J. 2010, *ApJ*, 717, 163
 Bradshaw, S. J., Klimchuk, J. A., & Reep, J. W. 2012, *ApJ*, 758, 53
 Bradshaw, S. J., & Viall, N. M. 2016, *ApJ*, 821, 63
 Cargill, P. J. 2014, *ApJ*, 784, 49C
 Cargill, P. J., & Klimchuk, J. A. 1997, *ApJ*, 478, 799
 Cargill, P. J., Warren, H. P., & Bradshaw, S. J. 2015, *RSPTA*, 373, 40260C
 Del Zanna, G., & Mason, H. E. 2003, *A&A*, 406, 1089
 Froment, C., Auchere, F., Bocchialini, K., et al. 2015, *ApJ*, 807, 158
 Guarrasi, M., Reale, F., & Peres, G. 2010, *ApJ*, 719, 576
 Guennou, C., Auchere, F., Klimchuk, J. A., Bocchialini, K., & Parenti, S. 2013, *ApJ*, 774, 31
 Klimchuk, J. A. 2006, *SoPh*, 234, 41
 Klimchuk, J. A. 2009, *ASPC*, 415, 221
 Klimchuk, J. A. 2015, *RSPTA*, 373, 20140256
 Klimchuk, J. A., Karpen, J. T., & Antiochos, S. K. 2010, *ApJ*, 714, 1239
 Klimchuk, J. A., Patsourakos, S., & Cargill, P. A. 2008, *ApJ*, 682, 1351
 Lemen, J., Title, A. M., Akin, D. J., et al. 2011, *SoPh*, 275, 17
 Lionello, R., Winebarger, A. R., Mok, Y., Linker, J. A., & Mikic, Z. 2013, *ApJ*, 773, 134
 Lopez Fuentes, M., & Klimchuk, J. A. 2015, *ApJ*, 799, 128
 Lopez Fuentes, M., & Klimchuk, J. A. 2016, *ApJ*, 828, 86
 Mikic, Z., Lionello, R., Mok, Y., Linker, J. A., & Winebarger, A. R. 2013, *ApJ*, 773, 94
 Mok, Y., Mikic, Z., Lionello, R., & Linker, J. 2008, *ApJ*, 679, 161
 Mulu-Moore, F. M., Winebarger, A. R., & Warren, H. P. 2011a, *ApJ*, 742, 6
 Mulu-Moore, F. M., Winebarger, A. R., Warren, H. P., & Aschwanden, M. J. 2011b, *ApJ*, 733, 59
 Parker, E. N. 1988, *ApJ*, 330, 474P
 Patsourakos, S., & Klimchuk, J. A. 2008, *ApJ*, 689, 1406
 Reale, F. 2014, *LRSP*, 11, 4
 Reep, J. W., Bradshaw, S. J., & Klimchuk, J. A. 2013, *ApJ*, 764, 193
 Schmelz, J. T., & Pathak, S. 2012, *ApJ*, 756, 126
 Schmelz, J. T., Pathak, S., Dhaliwal, R. S., Christian, G. M., & Fair, C. B. 2014, *ApJ*, 795, 139
 Tripathi, D., Klimchuk, J. A., & Mason, H. E. 2011, *ApJ*, 740, 111
 Ugarte-Urra, I., & Warren, H. P. 2012, *ApJ*, 761, 21
 Ugarte-Urra, I., & Warren, H. P. 2014, *ApJ*, 783, 12
 Ugarte-Urra, I., Warren, H. P., & Brooks, D. H. 2009, *ApJ*, 695, 642
 Ugarte-Urra, I., Winebarger, A. R., & Warren, H. P. 2006, *ApJ*, 643, 1245
 Vesecky, J. F., Antiochos, S. K., & Underwood, J. H. 1979, *ApJ*, 233, 987
 Viall, N. M., & Klimchuk, J. A. 2011, *ApJ*, 783, 24
 Viall, N. M., & Klimchuk, J. A. 2012, *ApJ*, 753, 35
 Viall, N. M., & Klimchuk, J. A. 2013, *ApJ*, 771, 115
 Viall, N. M., & Klimchuk, J. A. 2015, *ApJ*, 799, 58
 Viall, N. M., & Klimchuk, J. A. 2016, *ApJ*, 828, 76
 Warren, H. P., Brooks, D. H., & Winebarger, A. R. 2011, *ApJ*, 734, 90
 Warren, H. P., Kim, D. M., De Giorgi, A. M., & Ugarte-Urra, I. 2010, *ApJ*, 713, 1095
 Warren, H. P., Ugarte-Urra, I., Brooks, D. H., et al. 2007, *PASJ*, 59, 675
 Warren, H. P., Winebarger, A. R., & Brooks, D. H. 2012, *ApJ*, 759, 141
 Warren, H. P., Winebarger, A. R., & Hamilton, P. S. 2002, *ApJL*, 579, L41
 Warren, H. P., Winebarger, A. R., & Mariska, J. T. 2003, *ApJ*, 593, 1174
 Winebarger, A. R., Lionello, R., Downs, C., et al. 2016, *ApJ*, 831, 172
 Winebarger, A. R., Schmelz, J. T., Warren, H. P., Saar, S. H., & Kashyap, V. L. 2011, *ApJ*, 740, 2
 Winebarger, A. R., & Warren, H. P. 2005, *ApJ*, 626, 543
 Winebarger, A. R., Warren, H. P., & Seaton, D. B. 2003, *ApJ*, 593, 1164